

The physical and chemical structure of Sagittarius B2

VI. UCH_{II} regions in Sgr B2

F. Meng^{1,2}, Á. Sánchez-Monge², P. Schilke², A. Ginsburg³, C. DePree^{4,5}, N. Budaiev³, D. Jeff³, A. Schmiedeke⁶, A. Schwörer², V. S. Veena⁷, and Th. Möller²

¹ University of Chinese Academy of Sciences, Beijing 100049, People's Republic of China
 e-mail: mengfanyi@ucas.ac.cn, meng@ph1.uni-koeln.de

² I. Physikalisches Institut, Universität zu Köln, Zülpicher Str. 77, D-50937 Köln, Germany

³ Department of Astronomy, University of Florida, PO Box 112055, USA

⁴ NRAO, 520 Edgemont Rd, Charlottesville, VA, USA

⁵ Agnes Scott College, 141 E. College Ave., Decatur, GA 30030, USA

⁶ Max Planck Institute for Extraterrestrial Physics, Giessenbachstrasse 1, D-85748 Garching, Germany

⁷ Max Planck Institute for Radio Astronomy, Auf dem Hügel 69, D-53121 Bonn, Germany

Received ; accepted

ABSTRACT

Context.

The giant molecular cloud Sagittarius B2 (hereafter Sgr B2) is the most massive region with ongoing high-mass star formation in the Galaxy. Two ultra-compact H_{II} (UCH_{II}) regions were identified in Sgr B2's central hot cores, Sgr B2(M) and Sgr B2(N).

Aims. Our aim is to characterize the properties of the H_{II} regions in the entire Sgr B2 cloud. Comparing the H_{II} regions and the dust cores, we aim to depict the evolutionary stages of different parts of Sgr B2.

Methods. We use the Very Large Array in its A, CnB, and D configurations, and in the frequency band C (\sim 6 GHz) to observe the whole Sgr B2 complex. Using ancillary VLA data at 22.4 GHz and ALMA data at 96 GHz, we calculated the physical parameters of the UCH_{II} regions and their dense gas environment.

Results. We identify 54 UCH_{II} regions in the 6 GHz image, 39 of which are also detected at 22.4 GHz. Eight of the 54 UCH_{II} regions are newly discovered. The UCH_{II} regions have radii between 0.006 pc and 0.04 pc, and have emission measure between 10^6 pc cm⁻⁶ and 10^9 pc cm⁻⁶. The UCH_{II} regions are ionized by stars of types from B0.5 to O6. We found a typical gas density of $\sim 10^6 - 10^9$ cm⁻³ around the UCH_{II} regions. The pressure of the UCH_{II} regions and the dense gas surrounding them are comparable. The expansion timescale of these UCH_{II} regions is determined to be $\sim 10^4 - 10^5$ yr. The percentage of the dust cores that are associated with H_{II} regions are 33%, 73%, 4%, and 1% for Sgr B2(N), Sgr B2(M), Sgr B2(S), and Sgr B2(DS), respectively. Two-thirds of the dust cores in Sgr B2(DS) are associated with outflows.

Conclusions. The electron densities of the UCH_{II} regions we identified are in agreement with that of typical UCH_{II} regions, while the radii are smaller than those of the typical UCH_{II} regions. The dust cores in Sgr B2(M) are more evolved than in Sgr B2(N). The dust cores in Sgr B2(DS) are younger than in Sgr B2(M) or Sgr B2(N).

Key words. Stars: formation – Stars: massive – Radio continuum: ISM – Radio lines: ISM – ISM: clouds – ISM: individual objects: Sgr B2

1. Introduction

The giant molecular cloud Sagittarius B2 (Sgr B2) is the most massive ($\sim 10^7 M_{\odot}$) region with ongoing high-mass star formation in the Galaxy (see e.g., Goldsmith et al. 1990). Sgr B2 has a higher density ($> 10^5$ cm⁻³) and dust temperature ($\gtrsim 50 - 70$ K) compared to other star forming regions in the Galactic plane (see e.g., Ginsburg et al. 2016; Schmiedeke et al. 2016; Sánchez-Monge et al. 2017). Sgr B2 is located at a distance of 8.34 ± 0.16 pc, and only ~ 100 pc in projection from the Galactic center (Reid et al. 2014)¹. These features make Sgr B2 an excellent case to study high-mass star formation in an extreme high-

pressure environment. Such an environment resembles nearby starburst galaxies (Leroy et al. 2018). Understanding the structure of the Sgr B2 molecular cloud complex is necessary to comprehend the most massive star forming region in our Galaxy, which at the same time provides a unique opportunity to study in detail the nearest counterpart of the extreme environments that dominate star formation in the Universe (see, e.g., Kruijssen & Longmore 2013; Henshaw et al. 2022). This paper continues our series of studies on Sgr B2 (Schmiedeke et al. 2016; Sánchez-Monge et al. 2017; Pols et al. 2018; Schwörer et al. 2019; Meng et al. 2019). In Meng et al. (2019) we presented the observations of Sgr B2(DS), which is a part of Sgr B2 giant cloud, and analyzed the physical properties of the non-thermal emission within it. In this work we study the whole Sgr B2 region.

In the central 2 pc of Sgr B2 there are the two well-known and well-studied hot cores Sgr B2(N) and Sgr B2(M) (see, e.g.,

¹ A new distance to the Galactic center of 8.127 ± 0.031 kpc has been measured (Gravity Collaboration et al. 2018). For consistency with the papers published within the same series of studies of Sgr B2, we use the distance reported by Reid et al. (2014).

(Schmiedeke et al. 2016; Sánchez-Monge et al. 2017), which contain at least 70 high-mass stars with spectral types from O5 to B0 (see, e.g., Gaume et al. 1995; De Pree et al. 1998, 2014). Surrounding the two hot cores, there is a larger envelope (hereafter *the envelope*) with a radius of 20 pc that contains more than 99% of the total mass of Sgr B2 (Schmiedeke et al. 2016). Along with the active high-mass star forming activity discovered in Sgr B2(N) and Sgr B2(M), hints of star formation happening in the envelope are also revealed. Ginsburg et al. (2018), with ALMA at 3 mm, revealed 271 high-mass protostellar cores distributed throughout the entire Sgr B2 region, including the envelope. The luminosities of these dust cores suggest that they must contain objects with stellar masses higher than $8 M_{\odot}$.

Due to the high extinction in the infrared bands toward Sgr B2 (see Meng et al. 2019), there is no direct evidence of the existence of high-mass stars embedded in the dust cores detected by Ginsburg et al. (2018). However, since high-mass stars ionize the neutral material surrounding them, the presence and properties of the associated H_{II} regions reflect the evolutionary stages of these dust cores (see, e.g., González-Avilés et al. 2005; Breen et al. 2010). Additionally, since the free-free emission from H_{II} regions may extend from centimeter to millimeter wavelengths in the spectral domain (see, e.g., Sánchez-Monge et al. 2013), measuring the luminosities of the associated H_{II} regions can help us better constrain the luminosities of the dust cores. Therefore, to further characterize the evolutionary stages and physical properties of these dust cores, we investigate the possible H_{II} regions associated with them.

The H_{II} regions in Sgr B2 were targeted by several previous studies. Mehringer et al. (1993) observed the entire Sgr B2 with VLA in the 20, 6, and 3.6 cm bands and identified 15 H_{II} regions. The resolutions range from $\sim 20''$ to $\sim 3''$ when the wavelength changes from 20 to 3.6 cm, which correspond to the range 0.8–0.12 pc. The 15 H_{II} regions, except two unresolved cases, all have sizes $> 2''$. Since the 271 dust cores may contain newly formed high-mass stars (Ginsburg et al. 2018), the associated H_{II} regions may be ultra-compact H_{II} (UCH_{II}) and hyper-compact H_{II} (HCH_{II}) regions, which typically have sizes from ~ 0.03 pc to ~ 0.1 pc (see, e.g., Kurtz 2002; González-Avilés et al. 2005; Kurtz 2005; Breen et al. 2010). Thus, the resolution of Mehringer et al. (1993) is not sufficient to resolve the UCH_{II} and HCH_{II} regions. Gaume & Claussen (1990); Gaume et al. (1995) observed Sgr B2(N) and Sgr B2(M) at 7 mm and 1.3 cm and achieved resolutions of $0.065''$ and $0.25''$, respectively. Rolfs et al. (2011) observed Sgr B2(N) and Sgr B2(M) in 40 GHz with a resolution of $0.1''$. Unfortunately, these high-resolution observations do not cover the entire envelope. For example, Sgr B2(DS), where ~ 80 of dust cores reside (see, e.g., Ginsburg et al. 2018; Meng et al. 2019), is left out of these observations. LaRosa et al. (2000); Law et al. (2008a,b) also observed the entire Sgr B2 at centimeter wavelengths, but the resolutions were not high enough to study the UCH_{II} and HCH_{II} regions.

In this paper we present Very Large Array (VLA) observations of the entire Sgr B2 cloud in the frequency regime 4–8 GHz, with configurations A, BnC, and D. The high resolution ($\lesssim 0.01$ pc) and large spatial coverage (~ 20 pc) of our data sets make a systemic and complete study of the UCH_{II} and HCH_{II} regions in Sgr B2 possible. We also include analysis of the 3 mm image (Ginsburg et al. 2018) as well as the newly acquired SiO (5–4) data, both of which were observed with the Atacama Large Millimeter/submillimeter Array (ALMA). Thus, we can disentangle the contributions of ionized gas and dust at millimeter wavelengths and better constrain the evolutionary stages of the dust cores.

This paper is organized as follows. In Sect. 2 we describe the observations and the data reduction process. In Sect. 3 we present the results. In Sect. 4 we discuss the results. Finally, we summarize this paper in Sect. 6.

2. Observations and data reduction

We used the VLA in its A, CnB, and D configurations to observe the entire Sgr B2 complex in frequency band C (4–8 GHz). In the following we call this band 6 GHz. The observations with the CnB and D configurations were described in Meng et al. (2019). The observations with the A configuration were conducted from October 1 to 12, 2016 (project 16B-031, PI: F. Meng). We used 64 spectral windows with a bandwidth of 128 MHz each. Mosaic mode was used, with ten pointings for C band. The primary beam of each pointing is $7.5'$. Quasar 3C286 was used as the flux and bandpass calibrator, the SED of which is $S_{\nu} = 5.059 \pm 0.021 \text{ Jy} \times (S/8.435 \text{ GHz})^{-0.46}$ from 0.5 to 50 GHz (Perley & Butler 2013). Quasar J1820-2528, whose flux is 1.3 Jy in the C Band, was used as phase calibrator. The calibration was done using the standard VLA pipelines provided by the NRAO².

Calibration and imaging were done in Common Astronomy Software Applications (CASA 4.7.2 McMullin et al. 2007). The details of the data processing from the CnB and D configurations are described in Meng et al. (2019). The A configuration data were originally taken every 2 s. To shorten the time of processing, we applied `timebin` in CASA to the measurement sets, which averaged the data taken within 10 s into one data point. All the pointings of the mosaic in each band were primary beam corrected and the mosaic was imaged using the CASA task `tclean`. With a robust factor of 0, the image of C band has a synthesized beam of $0.62'' \times 0.28''$, with a position angle (PA) of 7.27° . The PA is defined positive north to east. To mitigate the spatial filtering effect of the A configuration image, we applied the `feather` algorithm to combine the images from A configuration and from CnB and D configurations. The combined image of the three configurations is shown in Fig. 1. The combined image has a resolution identical to that of the A configuration images, while being sensitive to spatial scales up to $\sim 240''$. The sensitivities of the observations are described in Sect. 3.

Ancillary data include the 22.4 GHz data, the 3 mm continuum, and SiO (5–4) data. The observations of the 22.4 GHz data are described in Gaume et al. (1995), with a resolution of $0.27'' \times 0.23''$ (PA = 70°). The root mean square (RMS) noise is 0.38 mJy/beam. The spatial coverage of the 22.4 GHz data is shown as the blue dashed box in Fig. 1. The 96 GHz continuum data covers the frequency range from 89.5 to 103.3 GHz. The image in 96 GHz has a resolution of $0.54'' \times 0.46''$ (PA = 68.31°), the observational details of which are described in Ginsburg et al. (2018). Unlike the 22.4 GHz image, the 96 GHz image covers the entire area shown in Fig. 1. The 22.4 GHz observations were performed 27 years prior to the 6 GHz and 96 GHz observations. If we assume that Sgr B2 has a proper motion of $\sim 50 \text{ km s}^{-1}$ (Henshaw et al. 2016), the corresponding position shift in 27 years is $0.04''$, which is only $\sim 10\%$ of the beam sizes of our images. In addition, we did not find any visible shift in the positions of the compact sources positions between the 6 and 22.4 GHz images. Thus, we do not take the astrometry difference into account when analyzing the 6 and 22.4 GHz data in the following sections. The SiO (5–4) emission was observed with ALMA

² The National Radio Astronomy Observatory is a facility of the National Science Foundation operated under cooperative agreement by Associated Universities, Inc.

(Project 2017.1.00114.S, P.I. A. Ginsburg) and has a resolution of $0.35'' \times 0.24''$, with PA of -80° , and spectral resolution of 1.35 km s^{-1} . For the details of the observation and data reduction, see Jeff et al. (in prep.). The typical RMS of the SiO image is 0.9 mJy/beam (0.3 K). The observation covers Sgr B2(S) and the eastern part of Sgr B2(DS).

3. Results

In this section we present the image of Sgr B2 at 6 GHz and the UCH_{II} regions identified in it. For the H_{II} regions, we calculated their actual sizes and physical properties using the observations at 6 GHz and at 22.4 GHz. With the 96 GHz data we characterized the properties of the dense gas that the UCH_{II} regions reside in.

3.1. Observed parameters of the 6 GHz sources

Figure 1 displays the image of Sgr B2 at 6 GHz, where the known large-scale H_{II} regions are denoted N, M, S, AA, DS, and V, following the nomenclature of Mehringer et al. (1992, 1993); Ginsburg et al. (2018); Meng et al. (2019). The maps at 22.4 GHz and 96 GHz are presented by Gaume et al. (1995) and Ginsburg et al. (2018), respectively. Our aim is to study UCH_{II} regions and since the 22.4 GHz image has non-complete spatial coverage, we performed compact source identification at the 6 GHz image only. We used the automatic source extracting algorithm SExtractor (Bertin & Arnouts 1996), which allows us to identify the location of bright compact sources throughout the map. We note that this algorithm also includes a large fraction of artificial sources due to some large-scale artifacts visible in the final image (see the zoomed-in images in Fig. 1). The variable noise (see Fig. A.1) also has an effect on the exclusion of certain sources with the automatic algorithms. After cross-checking the automatically produced lists of sources at 6 GHz and 22.4 GHz, we made the final catalog of continuum sources at 6 GHz by excluding or adding sources by visual inspection (in a similar way to the approach followed in Ginsburg et al. 2018 for the ALMA 96 GHz data). Since we focus on compact sources, extended emission larger than $5''$ or 0.2 pc (see contours in Fig. 1) are excluded in the catalog and the following analysis. In total, 54 compact sources are identified throughout the entire Sgr B2 cloud (see Table B.1), 8 of which are newly identified. Of these 54 cores, 8 are identified in Sgr B2(N), 40 in Sgr B2(M), 2 in Sgr B2(S), and 1 in Sgr B2(DS). All 54 compact sources are covered by the 22.4 GHz image, except core 1.

For each of the 54 compact sources we define a minimal circle that can include as much as the total flux density of it at 6 GHz.³ The observed radius of the core and the flux density within the core are denoted $r_{\text{obs}6}$ and S_6 , respectively. For these 54 sources we followed the same photometry procedure at the 22.4 GHz and 96 GHz bands, and obtained $r_{\text{obs}22}$, S_{22} , $r_{\text{obs}96}$, and S_{96} that correspond to the observed radii and flux densities. The observed radius and flux density in three bands of all the 54 compact sources are listed in Table B.1.

To match the sources across the three images (6, 22.4, and 96 GHz), we defined that if two sources in two images have a distance (distance between their centers) shorter than either of their radii, they are associated with each other. Afterward, we

manually adjust few of the matched sources in the crowded region in Sgr B2(M). For all the compact sources at 6 GHz, emission in the 96 GHz band is also detected. Among the 15 sources that have no S_{22} , 14 are without reliable 22.4 GHz detection ($S_{22} < 3\text{RMS}$), and one (#1 in Tab. B.1) is not spatially covered by the 22.4 GHz image. All the 22.4 GHz sources⁴ reported by Gaume et al. (1995) are associated with the 6 GHz compact sources.

We compared the spatial association of the 54 sources with the 271 dust cores identified at 96 GHz by Ginsburg et al. (2018). Although there is no one-to-one correspondence between the 271 dust cores and the associated dust emission of the 54 compact sources, we can still conclude that at least 217 (80%) dust cores are not associated with compact radio sources that are detectable with our sensitivity.

Most of the compact sources have $r_{\text{obs}6}$ from $0.5''$ to $1''$, which is comparable to the beam size at 6 GHz. Even though the 22.4 GHz image has higher resolution ($\sim 0.25''$), the measured $r_{\text{obs}22}$ are still not significantly larger than the beam size at 22.4 GHz. Therefore, most of the compact sources are not well resolved; in other words, $r_{\text{obs}6}$ or $r_{\text{obs}22}$ cannot accurately represent the actual radii of most of the compact sources. The 96 GHz compact sources, as indicated by Ginsburg et al. (2018), are also not resolved. The flux densities of the compact sources are distributed in a wide range; S_6 ranges from $\sim 3 \text{ mJy}$ to $\sim 300 \text{ mJy}$ at 6 GHz, as shown in Fig. 2. The mean and median of S_6 are 37.3 mJy and 16.2 mJy , respectively.

To test whether the nature of the emission at 6 and 22.4 GHz is free-free emission, we interpolated S_6 and S_{22} to derive a spectral index α_{6-22} for each of the 39 sources that have 22.4 GHz detection, see the last column of Table B.1. All 39 sources have $\alpha_{6-22} > -0.1$, which suggest that their emission at centimeter wavelengths is very probably dominated by thermal free-free emission from ionized gas (see, e.g., Sánchez-Monge et al. 2013). For the 15 sources without 22.4 GHz detections, we find that their S_6 are not higher than the values of the other sources. If we treat their emission at 6 GHz as free-free as well⁵, the derived physical parameters are also within the same ranges as the other sources (see Section 3.2). Thus, we treat all 54 sources as thermal free-free sources in the following analysis.

3.2. Physical parameters of the H_{II} regions

As we show in Sect. 3.1, most of the compact sources at 6 and 22.4 GHz are not well resolved. Therefore, we first need to determine their actual sizes. The observed flux density (S_6 and S_{22}) of an H_{II} region is related to its actual size (r_{calc} , which is called calculated radius in this paper), its electron temperature (T_e), and its emission measure (EM) as (see, e.g., Wilson et al. 2013)

$$\frac{S_\nu}{\text{mJy}} = 8.183 \times 10^{-4} \left(\frac{r_{\text{calc}}}{\text{arcsec}} \right)^2 \left(\frac{\nu}{\text{GHz}} \right)^2 \left(\frac{T_e}{\text{K}} \right) (1 - e^{-\tau_\nu}), \quad (1)$$

where the optical depth τ_ν is

$$\tau_\nu = 8.235 \times 10^{-2} \left(\frac{\nu}{\text{GHz}} \right)^{-2.1} \left(\frac{T_e}{\text{K}} \right)^{-1.35} \left(\frac{\text{EM}}{\text{pc cm}^{-6}} \right). \quad (2)$$

⁴ In Gaume et al. (1995), extended H_{II} regions are also included in the catalog. We only compare the compact sources ($r < 5''$) in their catalog with ours.

⁵ For single-dish images, the RMS around a certain null detection spot could be used to derive an upper limit of the possible signal, which in this paper can be translated into an upper limit of α_{6-22} ; however, because the artifacts in the 22.4 GHz image contain negative bowls of interferometric images, we do not trust the upper limits derived from the 22.4 GHz RMS map.

³ This is done by expanding the circle as long as the flux S_{total} within the circle increases monotonically. When S_{total} remains constant or (due to the “negative bowl” in the artifacts) decreases, the corresponding circle is called the minimum circle.

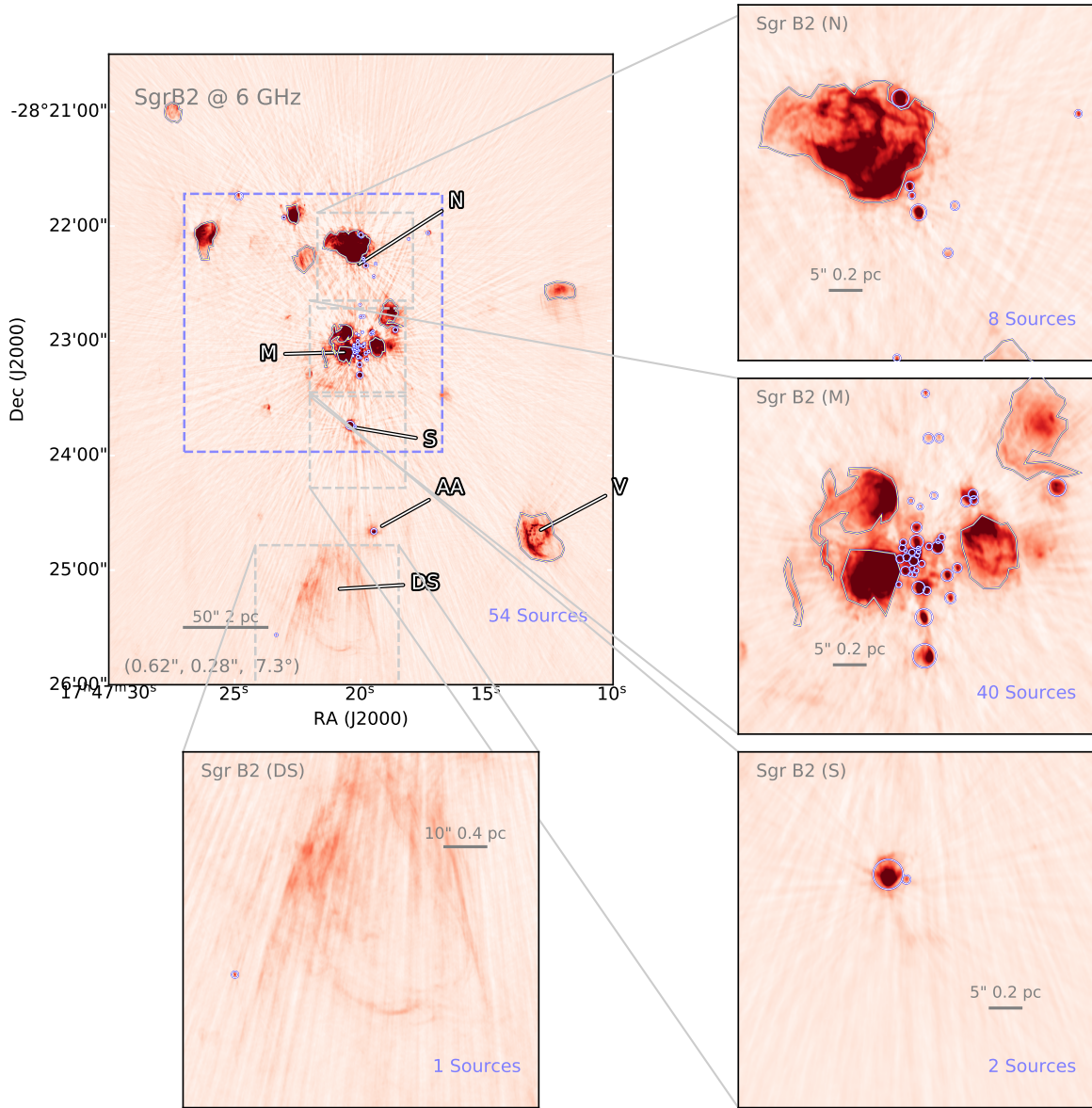


Fig. 1. Sources identified in the 6 cm image. Those objects shown as white and blue circles have radii of r_{obs6} (see Table B.1). Notable HII regions are indicated. The HII regions that are masked out for core identification are shown as white contours. The beam size is given in the lower left corner of the main panel ($\theta_{\text{maj}}, \theta_{\text{min}}, \text{PA}$). The spatial coverage of the 22.4 GHz image is shown as a blue dashed box.

In our case the frequency ν is 6 GHz or 22.4 GHz. We assume that T_e is 10^4 K, following the values given by [Mehringer et al. \(1993\)](#) for Sgr B2(N) and Sgr B2(M), considering that most of the compact sources are in these two regions. Thus, with the two independent flux density measurements, S_6 and S_{22} , we solve Eq. 1 and Eq. 2 to obtain r_{calc} and EM simultaneously for the 39 sources that are detected at both 6 and 22.4 GHz. For the 15 compact sources that are only detected at 6 GHz, we deconvolved the beam size from r_{obs6} to estimate r_{calc} , as $r_{\text{calc}}^2 + r_{\text{beam}}^2 = r_{\text{obs6}}^2$, and $r_{\text{beam}}^2 = 0.62'' \times 0.28''$ for 6 GHz. Then we calculated EM using the estimated r_{calc} . The r_{calc} and EM of all the compact sources are listed in Table B.2; those derived from the deconvolved r_{calc} are flagged with an asterisk (*) in Table B.2.

For all the compact sources that are associated with the 22.4 GHz detection, we plot the $r_{\text{obs6}} - r_{\text{calc}}$ diagram (see Fig. 3). We can see that in general r_{calc} follows the trend of deconvolu-

tion (i.e., $r_{\text{calc}}^2 = r_{\text{obs6}}^2 - 0.62'' \times 0.28''$), which suggests that the method we used to calculate r_{calc} , although without measuring the compact source size in the image, is in general consistent with the size we observed. The deviation between the r_{calc} from the dashed curve in Fig. 3 is likely due to some uncertainties in the observations and flux measurements. For example, the determination of r_{obs6} is made by including as much of the flux as possible, which might be larger than the actual observed size. In addition, due to the artifacts in the image, we cannot ideally define the boundaries of the compact sources, but only approximate the compact source as a circle with $r = r_{\text{obs}}$.

The probability distribution of EM of all the 54 compact sources is shown in Fig. 4. The EM of these compact sources ranges from $\sim 2 \times 10^6 \text{ pc cm}^{-6}$ to $\sim 3 \times 10^9 \text{ pc cm}^{-6}$. Only eight compact sources have $\text{EM} < 10^7 \text{ pc cm}^{-6}$, which means that most of the compact sources are consistent with the parameters derived for UCHII regions (see [Kurtz 2002](#)). From EM we es-

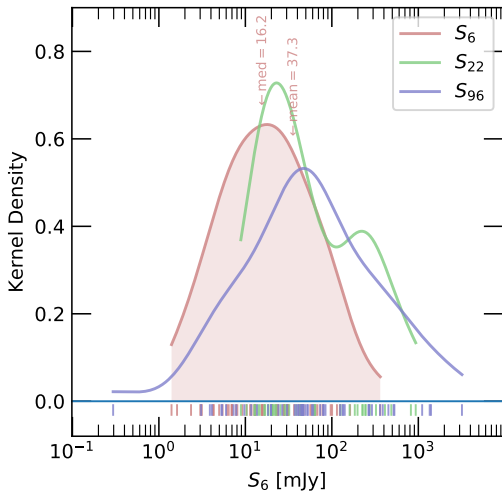


Fig. 2. Probability distribution of S_6 (pink), plotted as a kernel density estimation. Mean and median values are indicated. The distributions of S_{22} (green) and S_{96} (blue) are also shown.

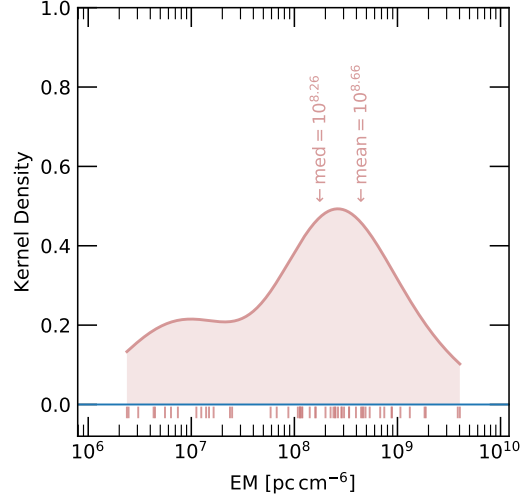


Fig. 4. Distribution of EM. The mean and median values are indicated.

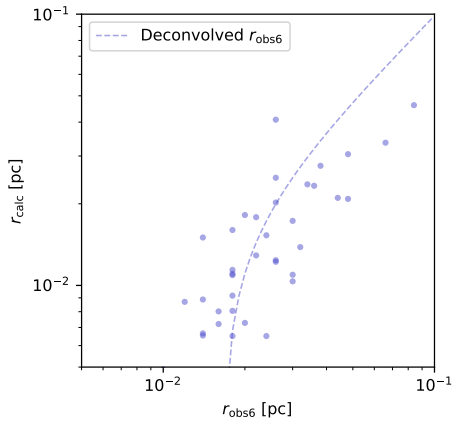


Fig. 3. Relation between $r_{\text{obs}6}$ and r_{calc} of the 39 compact sources with 22.4 GHz detection. The dashed curve indicates the deconvolution relationship $r_{\text{calc}}^2 + r_{\text{beam}}^2 = r_{\text{obs}6}^2$, where r_{beam} is the effective radius of the beam.

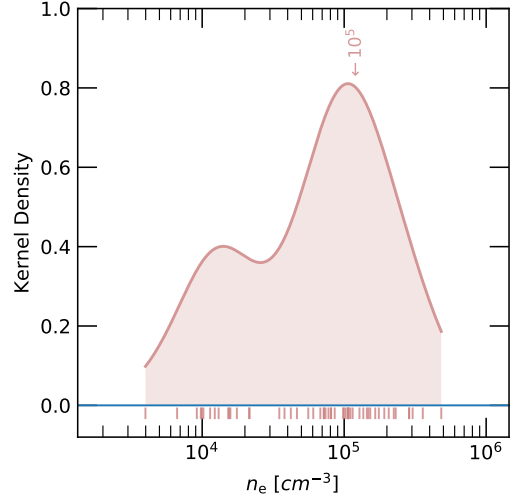


Fig. 5. Distribution of n_e . The mean and median values, which are both $\sim 10^5 \text{ cm}^{-3}$, are indicated.

estimated the electron density n_e as $n_e = [\text{EM}/(2r_{\text{calc}})]^{1/2}$. The distribution of n_e is shown in Fig. 5. The n_e of the 54 H α regions are from $\sim 4 \times 10^3 \text{ cm}^{-3}$ to $\sim 5 \times 10^5 \text{ cm}^{-3}$ with a mean value of $\sim 10^5 \text{ cm}^{-3}$.

Knowing EM, we calculated the flux of Lyman continuum photons (\dot{N}_{Ly}) that are needed to ionize these UCH α regions following Eq. C.18 in Schmiedeke et al. (2016). The derived \dot{N}_{Ly} ranges from 10^{46} s^{-1} to 10^{49} s^{-1} (see Fig. 6). If we assume that these cores are ionized by single stars, these UCH α regions are ionized by stars from spectral types B0.5 to O6 (Panagia 1973).

In this section we describe a method that is independent of the observed source size to derive the radius (r_{calc}) and emission measure (EM) of 39 sources detected at 6 and 22.4 GHz. To verify this a method, we compared the r_{calc} , EM, and \dot{N}_{Ly} values of these 39 sources with the values presented by Gaume et al. (1995), namely r_{G95} , EM_{G95} , and $\dot{N}_{\text{Ly G95}}$. Of the 39 sources, 33 are coincident with the UCH α regions reported by Gaume et al.

(1995). Twenty of the 33 sources have $r_{\text{calc}} > r_{\text{G95}}$ (see left panel of Fig. 7). The order of magnitude of EM of the UCH α regions is consistent in these two studies. Of the 33 sources, 23 have EM larger than EM_{G95} (see middle panel of Fig. 7). Most of the sources have \dot{N}_{Ly} similar to $\dot{N}_{\text{Ly G95}}$ (see right panel of Fig. 7), except source 44. The difference between \dot{N}_{Ly} and $\dot{N}_{\text{Ly G95}}$ of source 44 is possibly caused by the time-domain flickering of the radio emission in SgrB2 (see the last paragraph of this section).

In Fig. 8 we plot the diagram of r_{calc} and n_e . It is worth noting that all of the 39 H α regions have typical n_e of UCH α regions (i.e., $\sim 10^4 \text{ cm}^{-3}$ to $\sim 10^6 \text{ cm}^{-3}$; Kurtz 2005). However, 16 of these have r smaller than that of typical UCH α regions (~ 0.015 to $\sim 0.05 \text{ pc}$). Although some of the sources have sizes similar to HCH α regions, considering the low density of our H α regions compared to typical HCH α regions, and following the previous nomenclature of most of the sources (e.g., Gaume et al. 1995), we still call all the H α regions in this study UCH α regions.

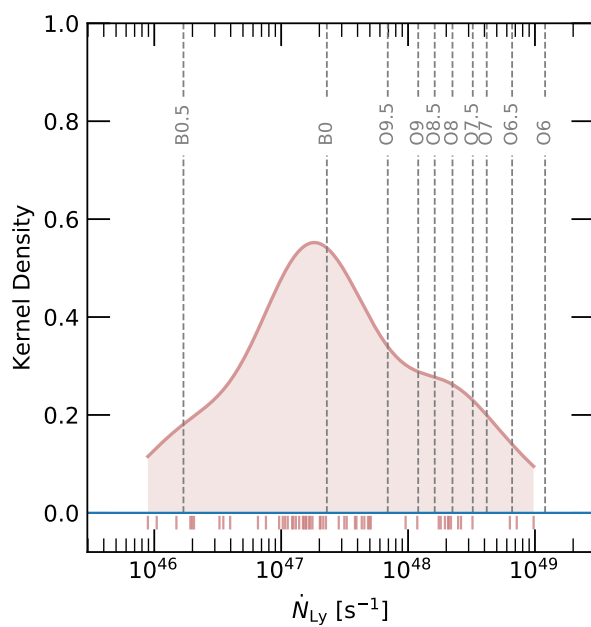


Fig. 6. Distribution of \dot{N}_{Ly} . The corresponding spectral type of the ionizing stars (assuming that the HII regions are ionized by single stars) are indicated.

Recently, Rivera-Soto et al. (2020) identified similar HII regions in W51 that have $n_e \sim 10^4 - 10^5 \text{ cm}^{-3}$ and $2 \times r \sim 10^{-3} - 10^{-2} \text{ pc}$. They categorized these sources as HCHII regions, but they are similar to smaller UCHII regions and are ionized by early B-type stars, which is in agreement with the spectral type of the ionizing stars for most of our UCHII regions (see Fig. 6). Unlike the HCHII regions in W51, our UCHII regions do not exactly follow the $r - n_e$ relationships of UCHII regions proposed by Garay & Lizano (1999) and Kim & Koo (2001), and have higher n_e (by a factor of ~ 2) than the predicted values (see Fig. 8). Such a discrepancy might be due to the neutral gas surrounding our UCHII regions that is denser ($n_{\text{H}_2} \gtrsim 10^6 \text{ cm}^{-3}$) than typical molecular cores ($n_{\text{H}_2} \sim 10^4 - 10^5 \text{ cm}^{-3}$; see, e.g., Bergin & Tafalla 2007). In Sect. 3.3 a detailed analysis of the gas density surrounding the UCHII regions is presented.

Since we cannot resolve the detailed morphologies of the UCHII regions, we neglect the possible inhomogeneity of the HII regions. The various morphologies of UCHII regions result in modified SEDs other than that described by Eq. 1 and Eq. 2, (see, e.g., Keto 2003; Keto et al. 2008). Additionally, if there are accretion flows to the HII regions, flickering of the flux on a timescale of $\sim 100 \text{ yr}$ may occur, which is observed by De Pree et al. (2014) and modeled by Peters et al. (2010b,c). Since the 6 GHz observation (2013) was performed 23 years after the 22.4 GHz observations (1989), the effects of flickering could be present in some of these cores. Hence, the simultaneous use of 6 GHz and 22.4 GHz fluxes may not be appropriate for the analysis of some sources. However, De Pree et al. (2014) reported the flickering of 4 out of 41 sources in Sgr B2 within a similar time range (1989–2014). Such a rarity of cases (10%) suggests that the flickering may not significantly alter our statistical results.

3.3. Dense gas environment

We extrapolated the HII regions' SED (Eq. 1) to subtract the free-free contribution from S_{96} to get the emission purely from dust, which is denoted S_{dust} . Twelve UCHII regions have S_{dust} below $3 \times \text{rms}$, while the other 42 UCHII regions have detectable dust emission after subtraction of the free-free emission. Using S_{dust} , we evaluated the dust properties in the vicinity of the 42 UCHII regions.

Following Ossenkopf & Henning (1994), we calculated the dust column density N_{d} as

$$S_{\text{dust}} = \frac{2h\nu^3}{c^2} \frac{1}{e^{\frac{h\nu}{k_B T_{\text{d}}}} - 1} \left(1 - e^{-\kappa_0 \left(\frac{\nu}{\nu_0} \right)^\beta N_{\text{d}}} \right) \frac{\pi r^2}{D^2}, \quad (3)$$

in which T_{d} is the dust temperature, D is the distance of Sgr B2, and r is the radius of the dust core. Since most of the dust cores are not resolved (Ginsburg et al. 2018), here we use $r = (r_{\text{obs96}}^2 - r_{\text{beam}}^2)^{1/2}$, where $r_{\text{beam}} = (0.54'' \times 0.46'')^{1/2}$ is the effective radius of the 96 GHz beam. The dust parameters κ_0 and β depend on the dust grain properties. Due to the general high temperature and high density of neutral gas revealed by previous studies (see, e.g., Hüttemeister et al. 1993; Schmiedeke et al. 2016), we assume that $T_{\text{d}} = 100$, $\kappa_0 = 2.631$, and $\beta = 1.05$ for $\nu_0 = 100 \text{ GHz}$. The assumption of κ_0 and β corresponds to dust grains without ice mantles and with a volume density of 10^8 cm^{-3} . We assume a gas-to-dust mass ratio of 100 (Ott et al. 2014; Giannetti et al. 2017) to estimate the gaseous mass N_{H_2} , $N_{\text{H}_2} = 100N_{\text{d}}$.

From the column density of molecular gas, N_{H_2} , we obtain the volume density of molecular gas (H_2),

$$n_{\text{H}_2} = \frac{3N_{\text{H}_2}}{4r}. \quad (4)$$

We list the n_{H_2} values at the position of the 42 UCHII regions associated with dust emission in Table B.2. The distribution of n_{H_2} is shown in Fig. 9. The n_{H_2} ranges from $\sim 10^6$ to $\sim 10^8 \text{ cm}^{-3}$. Due to the artifacts and possible small size of the dust core, even a dust core with enough volume density might not be detected by the sensitivity of our data set. We used the method in Ginsburg et al. (2018) to estimate the detection limit of the dust emission. Compared to the typical n_{H_2} of the molecular clouds surrounding UCHII regions (10^5 cm^{-3}) (e.g., Wood & Churchwell 1989), our UCHII regions reside in denser neutral gas. The median value obtained in this work is similar to the value ($2 \times 10^7 \text{ cm}^{-3}$) measured in the central region of Sgr B2(M) (de Pree et al. 1995; Hüttemeister et al. 1995; Sánchez-Monge et al. 2017), although our sources are also distributed in the outskirts of Sgr B2(M).

4. Analysis and discussion

4.1. Expansion and equilibrium

Based on the physical properties of the HII regions (see Sect. 3.2) and the properties of their surrounding environment (see Sect. 3.3), we now investigate the expansion time for these extremely compact and dense HII regions. The density of the molecular cloud that UCHII regions expand into significantly affects the expansion rate (e.g., Wood & Churchwell 1989; de Pree et al. 1995; De Pree et al. 1998). For the simple case of a spherical UCHII region ionized by the Lyman continuum flux of \dot{N}_{Ly} and expanding in molecular gas with volume density n_{H_2} and electron temperature of 10^4 K , following de Pree et al. (1995); De Pree et al. (1998) we calculate the initial Strömgren radius r_i

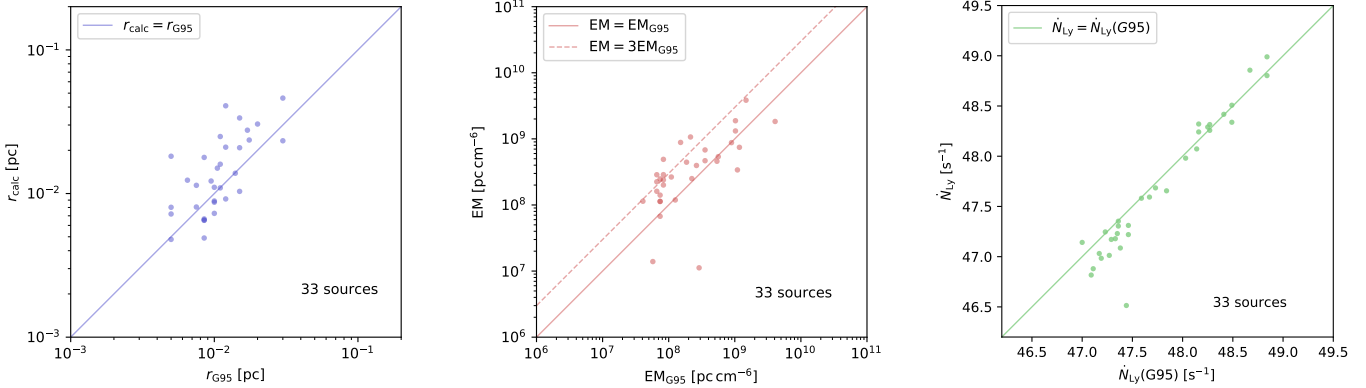


Fig. 7. Comparison between r_{calc} (left), EM (middle), and \dot{N}_{Ly} (right) of 33 sources and the corresponding parameters found by Gaume et al. (1995).

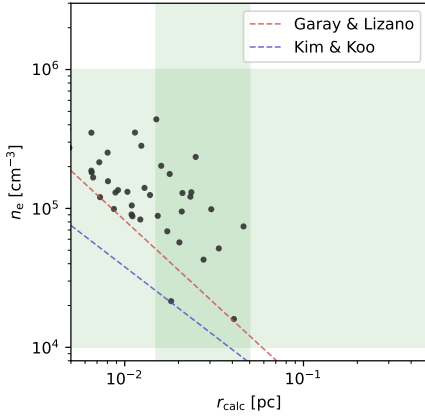


Fig. 8. Diagram of r_{calc} and n_e . Previously derived $r_{\text{calc}}-n_e$ relationships for UCHII regions from Garay & Lizano (1999), $n_e = 780 \times (2r)^{-1.19}$, and from Kim & Koo (2001), $n_e = 790 \times (2r)^{-0.99}$, are plotted as dashed lines. The green shading indicates the typical n_e of UCHII regions, which is from $\sim 10^4 \text{ cm}^{-3}$ to $\sim 10^6 \text{ cm}^{-3}$, and the typical r of UCHII regions, which is ~ 0.015 to ~ 0.05 pc (Kurtz 2005).

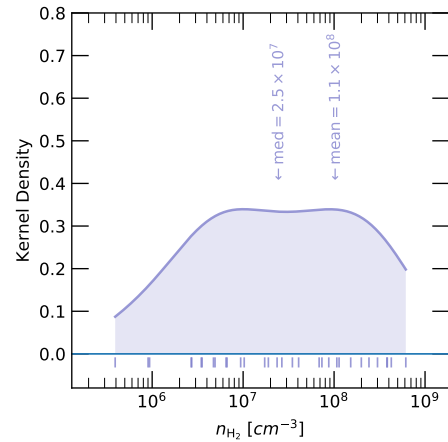


Fig. 9. Probability distribution of n_{H_2} of the dust surrounding the UCHII regions that are associated with dust emission. Median and mean values are indicated.

as

$$\frac{r_i}{\text{pc}} = 1.99 \times 10^{-2} \left(\frac{\dot{N}_{\text{Ly}}}{10^{49} \text{ s}^{-1}} \right)^{1/3} \left(\frac{n_{\text{H}_2}}{10^5 \text{ cm}^{-3}} \right)^{-2/3}. \quad (5)$$

For the 12 UCHII regions without detected associated dust emission (S_{dust} , which is S_{96} subtracting the free-free component), we assumed a uniform dust density of $2 \times 10^7 \text{ cm}^{-3}$ following De Pree et al. (2015). This value is in agreement with the median of n_{H_2} of the 42 sources that have physical S_{dust} . Since we assumed a relatively high gas density compared to typical dust cores (see, e.g., Bergin & Tafalla 2007), the nondetection of S_{dust} for 12 sources under such an assumption is due to small r but not low n_{H_2} . Then we calculated the expansion timescales of all 54 cores applying the expansion equation by Spitzer (1968); Dyson & Williams (1980),

$$r_{\text{calc}} = r_i \left(1 + \frac{7c_i t}{4r_i} \right)^{4/7}, \quad (6)$$

where c_i is the sound speed ($\sim 10 \text{ km s}^{-1}$). The expansion times, t , of the UCHII regions are listed in Table B.2. In Fig. 10 the cores are color-coded according to their t . In ideal cases most of the cores have an expansion time between 10^4 yr and 10^5 yr. The expansion times in this section were derived under the assumption of ideal conditions (Spitzer 1968). Such derived expansion times should be treated as lower limits and the actual expansion time might be longer for at least three reasons. First, the expansion of UCHII regions can be halted due to the pressure equilibrium between the ionized gas and the surrounding dense molecular gas (e.g., De Pree et al. 1998). We assume that T_e of the ionized gas is 10^4 K, and the molecular temperature T_{H_2} is from 50 K to 100 K. The pressure equilibrium condition ($2n_e T_e = n_{\text{H}_2} T_{\text{H}_2}$) can be expressed as $2n_e = 5 \times 10^{-3} n_{\text{H}_2}$ and $2n_e = 10^{-2} n_{\text{H}_2}$ for $T_{\text{H}_2} = 50$ K and 100 K, respectively. In dust cores with $n_{\text{H}_2} \gtrsim \times 10^7 \text{ cm}^{-3}$, the UCHII regions are mostly in equilibrium with the neutral gas, evident from Fig. 11, whereas for the lower n_{H_2} regime, the UCHII regions are in expansion phase owing to ionized gas pressure exceeding the neutral gas pressure. Second, in reality, dust absorption may reduce r_i , and therefore slows down the expansion (see, e.g., Wood & Churchwell 1989; De Pree et al. 1998). Third, accretion flow on to the

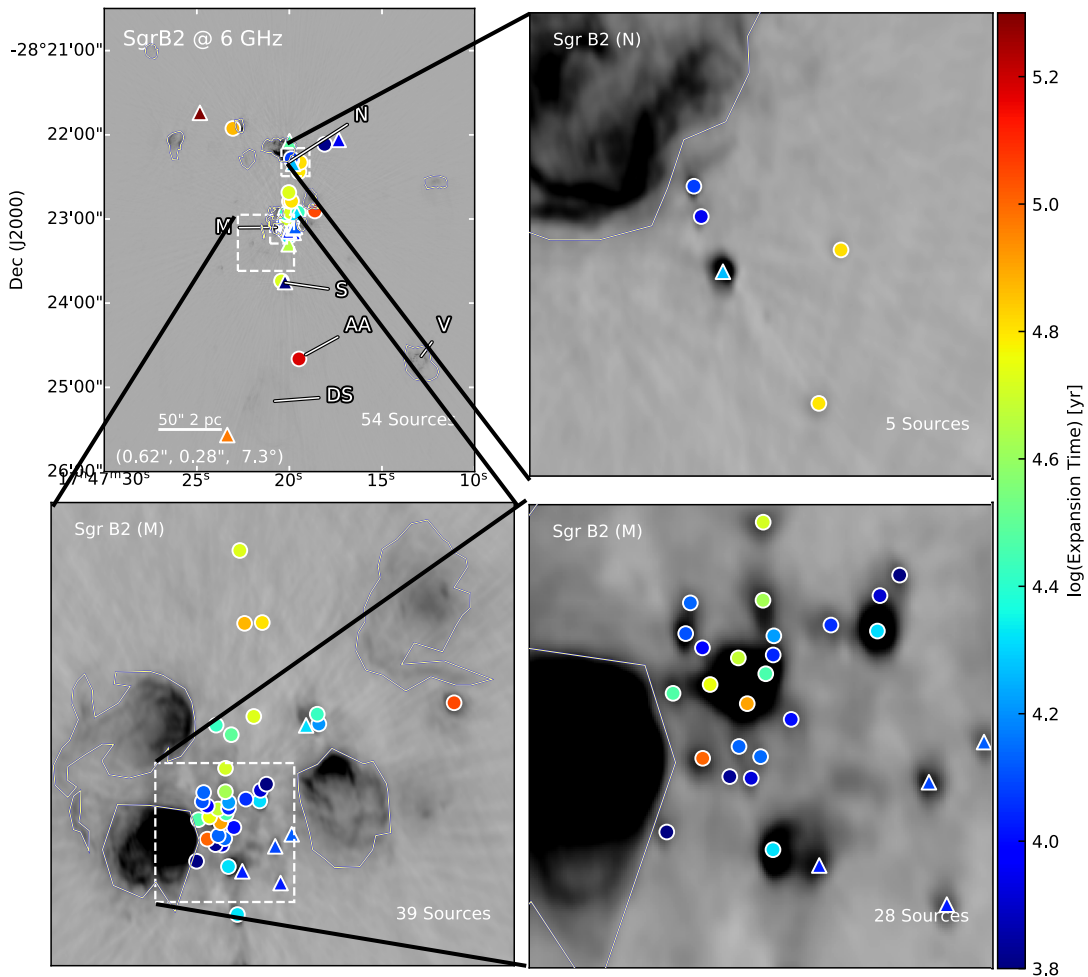


Fig. 10. Evolution sequence of the HII regions. The circles are calculated with the dust density derived from the 96 GHz image. The triangles are calculated with the dust density of $2 \times 10^7 \text{ cm}^{-3}$. The color of the markers indicates the expansion timescale.

Table 1. Number of objects associated with dust cores

Region	N	M	S	DS	Rest ^a	Total
Dust core	24	55	46	46	100	271
HII region	8	40	2	1	3	54
Outflow	— ^b	— ^b	— ^b	31	18 ^b	49 ^b
CH ₃ OH Maser	2	2	0	0	5	9

a: Rest of the envelope.

b: Not fully covered by the SiO map.

central star will disrupt the expansion process and cause a sudden decrease in the flux and size of the UCHII region. (see, e.g., Fig. 10 in Peters et al. 2010a). With the current data, we cannot quantify the effect of either of these mechanisms. Future observations, for example high-resolution radio recombination line observations, may provide constraints on the possible effect of accretion on the expansion of the HII regions.

4.2. Evolutionary stages

The type of objects that are associated with dust cores suggests the evolutionary stages of the dust cores in star formation activity. In Table 1 we summarize the type and number of objects associated with the dust cores in the subregions Sgr B2(N), Sgr B2(M), Sgr B2(S), and Sgr B2(DS), and in the rest of the envelope of Sgr B2.

Of all the 54 UCHII regions, 8 are in Sgr B2(N), 40 are in Sgr B2(M), 2 are in Sgr B2(S), 1 is in Sgr B2(DS) and 3 are in the rest of the envelope. Although the dust cores are distributed all over Sgr B2 (Ginsburg et al. 2018) and more than 80 of them are associated with the large HII region in Sgr B2(DS) (Meng et al. 2019), the dust cores are rarely associated with any UCHII regions outside of Sgr B2(N) and Sgr B2(M). The percentage of the dust cores that are associated with UCHII regions are 33%, 73%, 4%, and 1% for Sgr B2(N), Sgr B2(M), Sgr B2(S), and Sgr B2(DS), respectively, while for the remaining part of the envelope the percentage is 3%.

For a dust core, association with the HII region is a sign of that the core is more evolved (see, e.g., Breen et al. 2010). Therefore, the cores in Sgr B2(M) are the most evolved, while the cores in Sgr B2(S) and Sgr B2(DS) are the least evolved. The

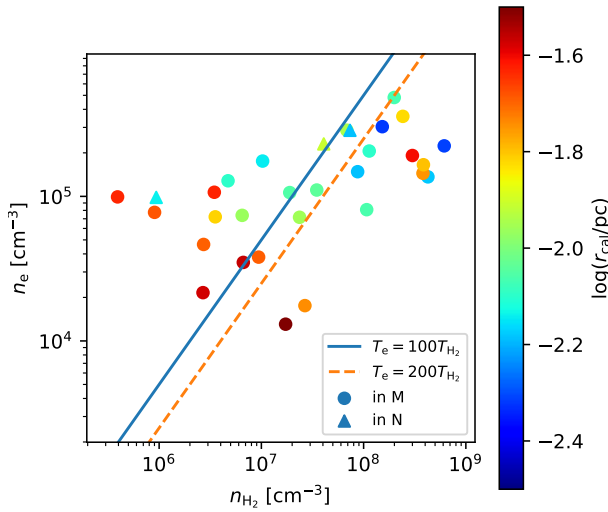


Fig. 11. Diagram of n_e and n_{H_2} . The H_{II} regions in Sgr B2(M) are shown as circles, while those in Sgr B2(N) are shown as triangles. The color indicates the size r_{calc} (see color scale at right). Equilibrium conditions are plotted as solid and dashed lines for $T_{H_2} = 100$ K and 50 K and thus for $T_e = 100T_{H_2}$ and $200T_{H_2}$.

evolutionary stages of the cores in Sgr B2(N) are between those of Sgr B2(M) and Sgr B2(DS) or Sgr B2(S).

All the dust cores in Sgr B2(DS) appear to be pure dust⁶. With the sensitivity of our observation (~ 1 mJy, for unresolved sources), we constrain the age of the possibly undetectable embedded H_{II} regions in the dust cores. We consider the \dot{N}_{Ly} from the central star are of 10^{46} , 10^{47} , 10^{48} s⁻¹, and dust densities are 10^6 and 10^8 cm⁻³, which are based on the typical values of the detected UCH_{II} regions. The evolution of S_6 of the H_{II} regions, based on the expansion model in Sect. 4.1 and Eq. 8 in (De Pree et al. 1998), are displayed in Fig. 12. The temporal evolution of r and EM leads to increase in S_6 (see Eq. 1). For the dust cores that have $n_{H_2} = 10^6$ cm⁻³, the embedded H_{II} regions with $\dot{N}_{\text{Ly}} \geq 10^{47}$ s⁻¹ will be observable ~ 100 yr after their birth, which contradicts the nondetection of H_{II} regions in Sgr B2(DS). For the dust cores that have $n_{H_2} = 10^8$ cm⁻³, the embedded H_{II} regions with $\dot{N}_{\text{Ly}} \geq 10^{47}$ s⁻¹ will be observable $\sim 10^3$ yr after their birth, which suggests that it is possible that the H_{II} regions are already formed but still too dim to be detected. The H_{II} regions with $\dot{N}_{\text{Ly}} \leq 10^{46}$ s⁻¹ will be always undetectable with the current sensitivity. The sizes of the embedded H_{II} regions will reach the typical size of the UCH_{II} regions in this study (~ 0.01 pc) in 10^4 years (de Pree et al. 1995, see Fig. 1 in). Thus, it is possible that stars later than B1 have already formed and ionized the interiors of the dust cores.

Collimated outflows are the footprints of the very early stages of star formation activity (see, e.g., Beuther et al. 2002). Outflows can be traced by SiO emission (e.g., Schilke et al. 1997). In a recent project, the SiO (5–4) emission was observed with ALMA (P.I. A. Ginsburg). For the details of the observa-

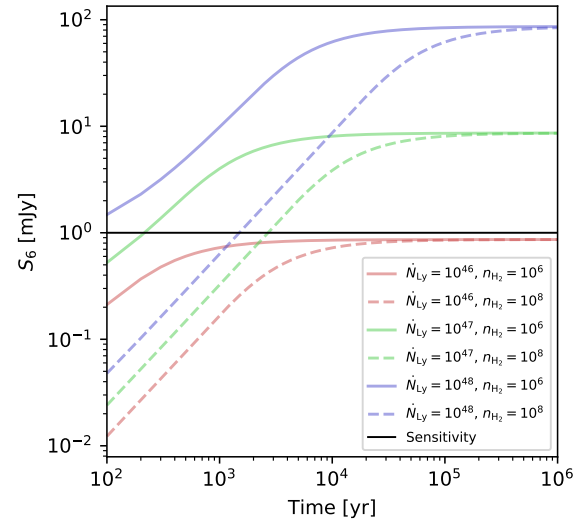


Fig. 12. Modeled evolution of S_6 of H_{II} regions with time. The black line denotes the sensitivity of our 6 GHz observation, which is ~ 1 mJy, for unresolved sources.

tion and data reduction, see Jeff et al. (in prep.). The resolution is $0.35'' \times 0.24''$, with P.A. of -80° . The spectral resolution is 1.35 km s⁻¹. The typical RMS of the image is 0.9 mJy/beam. The observation covers Sgr B2(S) and the eastern part of Sgr B2(DS). The peak intensity map of SiO (5–4) is shown in Figure C.1. Due to the artifacts around Sgr B2(S), we only analyzed the part of the image with declination $< -28:24:00$. We generated the moment one map by masking out all the pixels below 3σ (see Fig. C.2). The average velocity difference between the blueshifted and redshifted lobes is found to be ~ 10 km s⁻¹. We visually matched the positions of the dust cores identified by Ginsburg et al. (2018) and the SiO outflows. The dust cores that are 1) spatially associated with an outflow, 2) covered by the SiO image not associated with an outflow, and 3) not covered by the SiO image are indicated in Table B.3. Spatially, most of the outflows are associated with dust cores. On the other hand, of all the 120 dust cores covered by the SiO image, 49 are identified as associated with outflows. Particularly, among all the cores in Sgr B2(DS), two-thirds are associated with outflows. Such a high fraction confirms that the cores in Sgr B2(DS) are at their very early evolutionary stages.

CH₃OH masers serve as additional probes to trace the star formation activity (see, e.g., Breen et al. 2010). We cross-matched the CH₃OH masers presented by Caswell et al. (2010) with our dust cores⁷. In Table 1 the number of masers that are associated with the dust cores that are in each region are listed. The cores in Sgr B2(M) and in Sgr B2(N) are associated with two CH₃OH masers. The cores in Sgr B2(DS) have no associated masers. This lack of associated masers also suggests that the cores in Sgr B2(DS) are less evolved than those in Sgr B2(N) and Sgr B2(M).

It is worth noting that the dust cores in Sgr B2(DS) are distributed around the large-scale H_{II} region in Sgr B2(DS) (See Fig. 2 in Meng et al. 2019). The large-scale H_{II} region was ionized by a central O7 star and is still in the expansion phase

⁶ One H_{II} region is found associated with a core reported by Ginsburg et al. (2018), but the core emission is pure free-free, which suggests that the core is a dust-free H_{II} region. Therefore, no dust cores in Sgr B2(DS) are associated with H_{II} regions.

⁷ We searched for associated masers in a circle with a radius of 1 arcsec, which is double the beam size of the 96 GHz image.

(Meng et al. 2019). The expansion time of this HII region is $\sim 10^5$ yr, which is estimated based on the size of the HII region (0.72 pc) and the sound speed of the ionized gas, 10 km s^{-1} . This timescale, compared to the expansion time of the HII regions in Sgr B2(M) and Sgr B2(N) suggest that the central O7 star possibly formed before the stars in Sgr B2(M) and Sgr B2(N). Another possible scenario is that the O7 star was ejected from a nearby star forming site (e.g., Sgr B1) earlier than 10^5 yr ago, and Sgr B2 had no star forming activity at that time. The newly formed dust cores in Sgr B2(DS), on the other hand, are signs of star forming activity that possibly was triggered by the expansion of the large-scale HII region in Sgr B2(DS).

5. Summary

We observed the Sgr B2 complex with VLA A, BnC, and D array at 6 GHz and identified 54 compact radios sources. We found that 39 of the 54 sources are also detected in the 22.4 GHz band (Gaume et al. 1995). Our main results are summarized as follows:

- Using the 6 GHz data of all 54 sources, as well as the 22.4 GHz data of 39 sources, we calculated the EM, radius, electron densities, and the spectral type of the ionizing stars of all the 54 UCHII regions. The UCHII regions have radius between 6×10^{-3} pc and 4×10^{-2} pc, and have EM between 10^6 pc cm^{-6} and 10^9 pc cm^{-6} . We found that the electron densities of these UCHII regions are in agreement with the values of typical UCHII regions, while the radii are smaller than for the typical UCHII regions. We identified that the UCHII regions are ionized by stars with spectral types ranging between B0.5 to O6.
- Using the 96 GHz ALMA data, we characterized the dense gas environment where the UCHII regions are located. We found a typical dense gas density of $\sim 10^6 - 10^9 \text{ cm}^{-3}$ around the UCHII regions. Using Spitzer (1968), we estimated the expansion timescale of the UCHII regions as $\sim 10^4 - 10^5$ yr. More than half of the UCHII regions are close to equilibrium with the neutral gas; this means that the pressure of most UCHII regions and the dense gas surrounding them are comparable. Due to the high pressure of the neutral gas, some natal HII regions might be optically thick and cannot be detected with the sensitivity of this study. Instead, for the lower n_{H_2} regime ($n_{\text{H}_2} \lesssim \times 10^7 \text{ cm}^{-3}$) the ionized gas pressure exceeds that of the neutral gas and the UCHII regions are still expanding.
- The percentage of the dust cores that are associated with HII regions are 33%, 73%, 4%, and 1% for Sgr B2(N), Sgr B2(M), Sgr B2(S), and Sgr B2(DS), respectively. Among all the dust cores in Sgr B2(DS), two-thirds are associated with outflows that are traced by SiO(5–4). The dust cores in both of Sgr B2(M) and Sgr B2(N) are associated with two 6.7 GHz CH₃OH masers, while the dust cores in Sgr B2(DS) have no associated maser. Based on these findings, we suggest that the dust cores in Sgr B2(M) are more evolved than those in Sgr B2(N). The dust cores in Sgr B2(DS) are younger than those in Sgr B2(M) or Sgr B2(N).

In this work, we calculated the physical properties of the UCHII regions and their surrounding neutral gas in Sgr B2. We found that the pressure of the UCHII regions and the dense gas surrounding them are comparable. We also characterized the evolutionary stages of these UCHII regions and obtained their minimum expansion timescales.

Acknowledgements. FM, ASM, PS, ASchw research is carried out within the Collaborative Research Centre 956, sub-projects A6 and C3, funded by the Deutsche Forschungsgemeinschaft (DFG) - project ID 184018867. This research made use of Astropy,⁸ a community-developed core Python package for Astronomy (Astropy Collaboration et al. 2013, 2018).

References

Astropy Collaboration, Price-Whelan, A. M., Sipőcz, B. M., et al. 2018, AJ, 156, 123

Astropy Collaboration, Robitaille, T. P., Tollerud, E. J., et al. 2013, A&A, 558, A33

Benson, J. M. & Johnston, K. J. 1984, ApJ, 277, 181

Bergin, E. A. & Tafalla, M. 2007, ARA&A, 45, 339

Bertin, E. & Arnouts, S. 1996, A&AS, 117, 393

Beuther, H., Schilke, P., Sridharan, T. K., et al. 2002, A&A, 383, 892

Breen, S. L., Ellingsen, S. P., Caswell, J. L., & Lewis, B. E. 2010, MNRAS, 401, 2219

Caswell, J. L., Fuller, G. A., Green, J. A., et al. 2010, MNRAS, 404, 1029

De Pree, C. G., Goss, W. M., & Gaume, R. A. 1998, ApJ, 500, 847

De Pree, C. G., Peters, T., Mac Low, M. M., et al. 2014, ApJ, 781, L36

De Pree, C. G., Peters, T., Mac Low, M. M., et al. 2015, ApJ, 815, 123

de Pree, C. G., Rodriguez, L. F., & Goss, W. M. 1995, Rev. Mexicana Astron. Astrofis., 31, 39

Dyson, J. E. & Williams, D. A. 1980, Physics of the interstellar medium

Garay, G. & Lizano, S. 1999, PASP, 111, 1049

Gaume, R. A. & Claussen, M. J. 1990, ApJ, 351, 538

Gaume, R. A., Claussen, M. J., de Pree, C. G., Goss, W. M., & Mehringer, D. M. 1995, ApJ, 449, 663

Giannetti, A., Leurini, S., König, C., et al. 2017, A&A, 606, L12

Ginsburg, A., Bally, J., Barnes, A., et al. 2018, ApJ, 853, 171

Ginsburg, A., Henkel, C., Ao, Y., et al. 2016, A&A, 586, A50

Goldsmith, P. F., Lis, D. C., Hills, R., & Lasenby, J. 1990, ApJ, 350, 186

González-Avilés, M., Lizano, S., & Raga, A. C. 2005, ApJ, 621, 359

Gravity Collaboration, Abuter, R., Amorim, A., et al. 2018, A&A, 615, L15

Henshaw, J. D., Barnes, A. T., Battersby, C., et al. 2022, arXiv e-prints, arXiv:2203.11223

Henshaw, J. D., Longmore, S. N., Kruijssen, J. M. D., et al. 2016, MNRAS, 457, 2675

Huttemeister, S., Wilson, T. L., Mauersberger, R., et al. 1995, A&A, 294, 667

Huttemeister, S., Wilson, T. L., Henkel, C., & Mauersberger, R. 1993, A&A, 276, 445

Keto, E. 2003, ApJ, 599, 1196

Keto, E., Zhang, Q., & Kurtz, S. 2008, ApJ, 672, 423

Kim, K.-T. & Koo, B.-C. 2001, ApJ, 549, 979

Kruijssen, J. M. D. & Longmore, S. N. 2013, MNRAS, 435, 2598

Kurtz, S. 2002, in Astronomical Society of the Pacific Conference Series, Vol. 267, Hot Star Workshop III: The Earliest Phases of Massive Star Birth, ed. P. Crowther, 81

Kurtz, S. 2005, in IAU Symposium, Vol. 227, Massive Star Birth: A Crossroads of Astrophysics, ed. R. Cesaroni, M. Felli, E. Churchwell, & M. Walmsley, 111–119

LaRosa, T. N., Kassim, N. E., Lazio, T. J. W., & Hyman, S. D. 2000, AJ, 119, 207

Law, C. J., Yusef-Zadeh, F., & Cotton, W. D. 2008a, ApJS, 177, 515

Law, C. J., Yusef-Zadeh, F., Cotton, W. D., & Maddalena, R. J. 2008b, ApJS, 177, 255

Leroy, A. K., Bolatto, A. D., Ostriker, E. C., et al. 2018, ApJ, 869, 126

McMullin, J. P., Waters, B., Schiebel, D., Young, W., & Golap, K. 2007, in Astronomical Society of the Pacific Conference Series, Vol. 376, Astronomical Data Analysis Software and Systems XVI, ed. R. A. Shaw, F. Hill, & D. J. Bell, 127

Mehringer, D. M., Palmer, P., Goss, W. M., & Yusef-Zadeh, F. 1993, ApJ, 412, 684

Mehringer, D. M., Yusef-Zadeh, F., Palmer, P., & Goss, W. M. 1992, ApJ, 401, 168

Meng, F., Sánchez-Monge, Á., Schilke, P., et al. 2019, A&A, 630, A73

Ossenkopf, V. & Henning, T. 1994, A&A, 291, 943

Ott, J., Weiß, A., Staveley-Smith, L., Henkel, C., & Meier, D. S. 2014, ApJ, 785, 55

Panagia, N. 1973, AJ, 78, 929

Perley, R. A. & Butler, B. J. 2013, ApJS, 204, 19

Peters, T., Banerjee, R., Klessen, R. S., et al. 2010a, ApJ, 711, 1017

Peters, T., Klessen, R. S., Mac Low, M.-M., & Banerjee, R. 2010b, ApJ, 725, 134

⁸ <http://www.astropy.org>

Peters, T., Mac Low, M.-M., Banerjee, R., Klessen, R. S., & Dullemond, C. P. 2010c, *ApJ*, 719, 831

Pols, S., Schwörer, A., Schilke, P., et al. 2018, *A&A*, 614, A123

Reid, M. J., Menten, K. M., Brunthaler, A., et al. 2014, *ApJ*, 783, 130

Rivera-Soto, R., Galván-Madrid, R., Ginsburg, A., & Kurtz, S. 2020, *ApJ*, 899, 94

Rolffs, R., Schilke, P., Wyrowski, F., et al. 2011, *A&A*, 529, A76

Sánchez-Monge, Á., Kurtz, S., Palau, A., et al. 2013, *ApJ*, 766, 114

Sánchez-Monge, Á., Schilke, P., Schmiedeke, A., et al. 2017, *A&A*, 604, A6

Schilke, P., Walmsley, C. M., Pineau des Forets, G., & Flower, D. R. 1997, *A&A*, 321, 293

Schmiedeke, A., Schilke, P., Möller, T., et al. 2016, *A&A*, 588, A143

Schwörer, A., Sánchez-Monge, Á., Schilke, P., et al. 2019, *A&A*, 628, A6

Spitzer, L. J. 1968, *Interscience Tracts on Physics and Astronomy*, 28

Wilson, T., Rohlfs, K., & Hüttemeister, S. 2013, *Tools of Radio Astronomy, Astronomy and Astrophysics Library* (Springer Berlin Heidelberg)

Wood, D. O. S. & Churchwell, E. 1989, *ApJS*, 69, 831

Appendix A: RMS maps

The rms maps were generated using SExtractor (Bertin & Arnouts 1996). Although the core identification was performed by eye, SExtractor produces rms maps as side-products of automated core identification. The rms maps are shown in Fig. A.1.

Appendix B: Tables

Appendix C: SiO Images

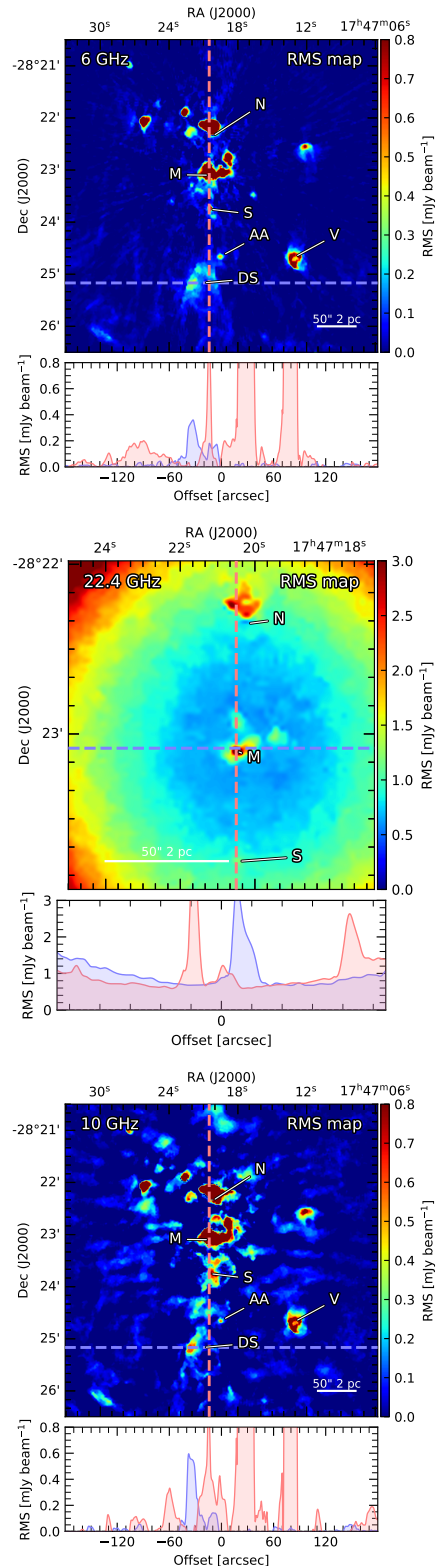


Fig. A.1. RMS maps of 6 GHz, 22.4 GHz, and 96 GHz. The resolutions are given in Sect. 2. Each image has two profile cuts, in blue and red. To better show the features and maxima of the rms of each image, the offset is different for each of the three images. The offset of each profile increases from left to right and from bottom to top. The profile is below each image.

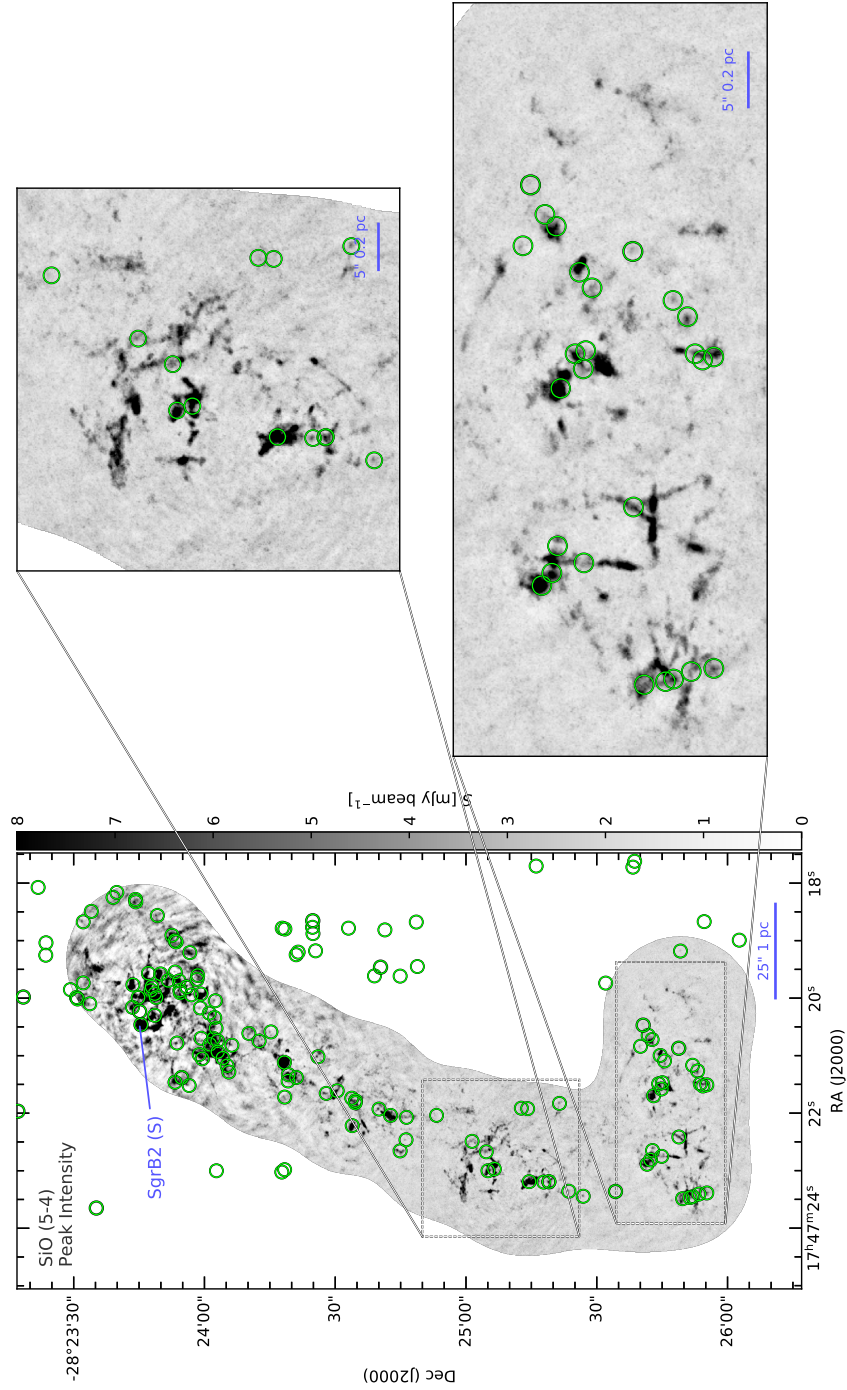


Fig. C.1. Peak intensity map of SiO (5-4) line. The zoomed-in plots are the regions in SgrB2(DS) with abundant outflows. The resolution of the image is $0.35'' \times 0.24''$, with P.A. of -80° . The dust cores identified by Ginsburg et al. (2018) are shown as green circles, whose size is not scaled to the size of the cores.

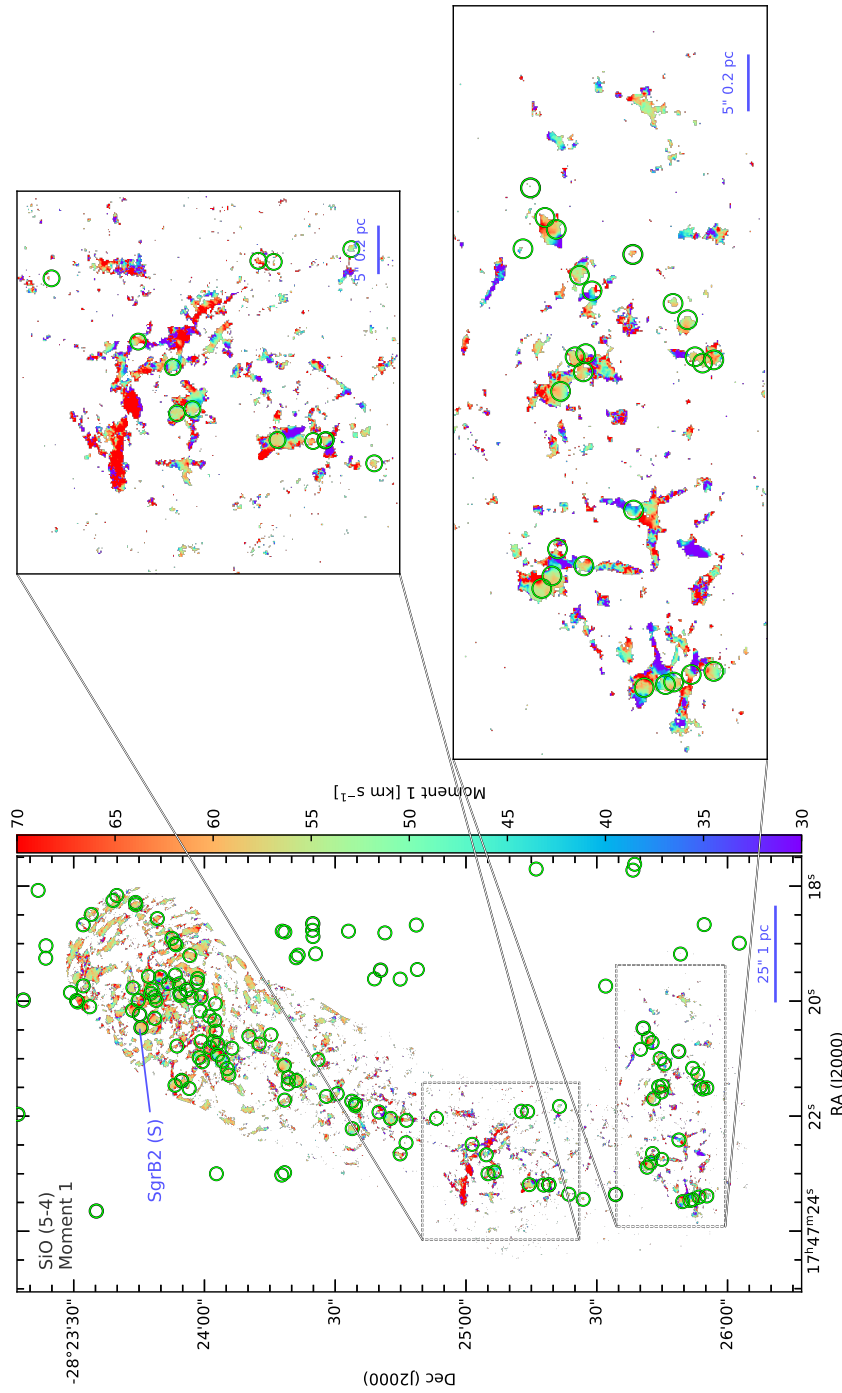


Fig. C.2. Moment 1 map of SiO (5-4) line. The zoomed-in plots are the regions in Sgr B2(DS) with abundant outflows. The resolution of the image is $0.35'' \times 0.24''$, with P.A. of -80° . The dust cores identified by Ginsburg et al. (2018) are shown as green circles, whose size is not scaled to the size of the cores.

Table B.1. Observed parameters

#	RA 17:47:--	DEC -28:--	$r_{\text{obs}6}$ arcsec	S_6 mJy	$r_{\text{obs}22}$ arcsec	S_{22} mJy	$r_{\text{obs}96}$ arcsec	S_{96} mJy	α_{6-22}
1*	23.355	25:33.95	0.70	2.4 ± 0.1	0.35	0.3 ± 0.2	...
2 ^a	19.485	24:39.75	1.45	64.9 ± 0.3	1.20	60.9 ± 0.2	...
3*	20.235	23:44.95	0.60	7.0 ± 0.1	0.60	14.7 ± 0.7	0.60	7.9 ± 0.2	0.56 ± 0.26
4 ^a	20.428	23:44.25	2.10	363.1 ± 0.8	1.15	820.5 ± 1.6	1.45	1107.6 ± 0.5	0.62 ± 0.27
5 ^a	20.042	23:18.00	1.65	123.8 ± 0.2	1.10	160.4 ± 0.9	1.05	135.5 ± 0.2	0.20 ± 0.09
6 ^a	20.049	23:12.60	1.20	68.1 ± 0.2	0.65	126.1 ± 0.7	0.80	124.8 ± 0.2	0.47 ± 0.21
7 ^b	19.765	23:09.90	0.75	15.6 ± 0.1	0.50	22.8 ± 0.7	0.40	18.3 ± 0.2	0.29 ± 0.13
8*	20.015	23:08.85	0.55	28.3 ± 0.3	0.55	64.2 ± 0.7	0.55	52.5 ± 0.6	0.62 ± 0.27
9 ^a	20.106	23:08.45	0.90	96.9 ± 0.5	0.70	274.6 ± 0.7	0.75	266.3 ± 1.1	0.79 ± 0.35
10 ^b	20.315	23:08.00	0.40	9.2 ± 0.6	0.30	25.5 ± 0.7	0.45	37.3 ± 0.9	0.77 ± 0.35
11 ^b	19.799	23:06.70	0.80	31.3 ± 0.3	0.60	63.3 ± 0.7	0.55	39.0 ± 0.3	0.53 ± 0.24
12 ^b	20.148	23:06.60	0.35	7.0 ± 0.4	0.30	14.1 ± 0.7	0.35	44.0 ± 1.1	0.53 ± 0.25
13 ^b	20.193	23:06.55	0.30	4.2 ± 0.4	0.30	20.3 ± 0.7	0.40	132.9 ± 1.6	1.20 ± 0.54
14 ^b	20.246	23:06.10	0.65	30.9 ± 1.0	0.45	28.4 ± 1.1	0.45	46.4 ± 3.0	-0.06 ± 0.07
15 ^b	20.133	23:06.05	0.35	6.9 ± 0.4	0.25	12.7 ± 0.7	0.30	59.0 ± 1.0	0.46 ± 0.23
16 ^b	20.174	23:05.80	0.40	11.8 ± 0.6	0.30	45.9 ± 0.8	0.50	267.1 ± 1.9	1.03 ± 0.46
17 ^b	19.693	23:05.65	0.65	15.9 ± 0.3	0.40	20.2 ± 0.7	0.40	13.6 ± 0.2	0.18 ± 0.10
18 ^b	20.072	23:05.10	0.45	12.7 ± 0.4	0.30	22.0 ± 0.7	0.40	45.5 ± 1.5	0.42 ± 0.19
19 ^{ab}	20.159	23:04.70	0.65	114.6 ± 0.8	0.60	932.9 ± 1.3	0.70	3194.7 ± 2.8	1.59 ± 0.70
20 ^{ab}	20.303	23:04.40	0.55	27.5 ± 1.0	0.55	52.3 ± 2.7	...
21 ^{ab}	20.231	23:04.20	0.55	58.4 ± 0.8	0.40	245.2 ± 0.9	0.40	528.6 ± 1.7	1.09 ± 0.48
22 ^a	20.121	23:03.90	0.35	41.5 ± 0.3	0.45	487.2 ± 0.9	0.50	1353.7 ± 2.0	1.87 ± 0.82
23 ^a	20.174	23:03.50	0.45	47.1 ± 0.4	0.40	225.3 ± 0.8	0.40	517.8 ± 1.5	1.19 ± 0.52
24 ^{ab}	20.106	23:03.40	0.30	15.5 ± 0.3	0.40	450.9 ± 1.6	...
25 ^{ab}	20.246	23:03.25	0.25	4.3 ± 0.3	0.25	12.9 ± 0.7	0.30	80.9 ± 1.1	0.83 ± 0.38
26 ^b	20.106	23:02.90	0.30	8.1 ± 0.2	0.30	10.3 ± 0.7	0.35	47.2 ± 1.2	0.18 ± 0.12
27 ^{ab}	20.277	23:02.85	0.45	24.0 ± 0.4	0.45	198.2 ± 0.8	0.50	387.9 ± 1.5	1.60 ± 0.70
28 ^{ab}	19.902	23:02.80	0.85	100.7 ± 0.3	0.60	323.9 ± 0.8	0.85	360.2 ± 0.6	0.89 ± 0.39
29 ^b	19.992	23:02.65	0.45	13.1 ± 0.2	0.40	17.0 ± 0.7	0.40	19.8 ± 0.7	0.20 ± 0.10
30 ^b	20.269	23:02.05	0.45	13.0 ± 0.3	0.30	16.6 ± 0.7	0.45	44.4 ± 1.0	0.19 ± 0.10
31 ^{ab}	20.125	23:02.00	0.95	56.3 ± 0.6	0.55	62.1 ± 0.9	0.55	73.3 ± 1.3	0.07 ± 0.04
32 ^b	19.898	23:01.90	0.35	11.3 ± 0.1	0.30	18.5 ± 0.7	0.45	40.5 ± 0.2	0.37 ± 0.17
33 ^b	19.860	23:01.35	0.45	10.4 ± 0.1	0.30	19.8 ± 0.7	0.45	24.1 ± 0.2	0.49 ± 0.22
34 ^b	20.125	22:60.00	0.70	22.7 ± 0.3	0.75	41.6 ± 0.5	...
35*	20.087	22:57.05	0.40	1.6 ± 0.1	0.50	5.3 ± 0.2	...
36 ^a	19.598	22:56.25	0.75	30.9 ± 0.2	0.70	38.7 ± 0.7	0.55	26.7 ± 0.2	0.17 ± 0.08
37 ^a	20.186	22:56.25	0.40	3.1 ± 0.1	0.40	3.9 ± 0.2	...
38 ^a	19.515	22:56.15	0.60	30.3 ± 0.2	0.40	44.2 ± 0.7	0.55	49.6 ± 0.2	0.29 ± 0.13
39*	19.939	22:55.50	0.50	1.4 ± 0.1	0.50	3.1 ± 0.2	...
40 ^a	19.526	22:55.30	0.65	36.6 ± 0.1	0.40	43.0 ± 0.7	0.55	45.6 ± 0.2	0.12 ± 0.06
41 ^a	18.629	22:54.30	1.25	73.9 ± 0.5	1.15	84.5 ± 0.3	...
42*	20.000	22:47.45	0.70	5.4 ± 0.1	0.70	6.0 ± 0.2	...
43*	19.886	22:47.40	0.60	3.1 ± 0.1	0.60	5.4 ± 0.2	...
44 ^b	20.030	22:41.15	0.50	5.0 ± 0.1	0.35	32.2 ± 0.7	0.55	79.0 ± 0.2	1.41 ± 0.62
45 ^b	19.489	22:26.40	0.65	6.1 ± 0.1	0.80	11.7 ± 0.2	...
46 ^a	19.803	22:20.70	1.10	79.1 ± 0.1	0.65	227.5 ± 0.8	0.50	141.0 ± 0.4	0.80 ± 0.35
47*	19.417	22:19.75	0.60	3.0 ± 0.1	0.60	7.3 ± 0.2	...
48 ^a	19.871	22:18.30	0.45	7.8 ± 0.1	0.30	43.5 ± 0.7	0.95	1401.0 ± 5.4	1.30 ± 0.57
49 ^a	19.898	22:17.00	0.65	28.2 ± 0.4	0.45	184.2 ± 0.7	0.50	290.9 ± 3.1	1.42 ± 0.63
50 ^b	18.102	22:06.85	0.50	6.4 ± 0.1	0.25	8.9 ± 0.7	0.50	9.7 ± 0.2	0.25 ± 0.15
51 ^a	19.996	22:04.65	1.20	162.6 ± 0.9	0.80	411.3 ± 1.5	1.00	271.4 ± 0.6	0.70 ± 0.31
52 ^a	17.337	22:03.60	0.75	16.5 ± 0.1	0.45	29.8 ± 1.1	0.65	19.8 ± 0.2	0.45 ± 0.20
53 ^b	23.049	21:55.55	0.85	23.6 ± 0.1	0.90	30.3 ± 0.2	...
54 ^a	24.830	21:44.34	1.95	20.6 ± 0.1	0.45	4.1 ± 0.2	...

a: Associated with the HII regions identified by Benson & Johnston (1984).

b: Associated with the HII regions identified by Gaume et al. (1995).

*: Newly identified in this study.

Table B.2. Derived parameters

#	r_{calc} $\times 10^{-3}$ pc	EM_{calc} $\times 10^7$ pc cm $^{-6}$	$\log_{10}(\dot{N}_{\text{Ly}}/\text{s}^{-1})$	n_e $\times 10^4$ cm $^{-3}$	n_{H_2} $\times 10^6$ cm $^{-3}$	r_i $\times 10^{-3}$ pc	t $\times 10^4$ yrs
1	*26.73	*0.24	*46.17	*0.94	...	*0.106	*9.3
2	*57.40	*1.49	*47.64	*1.61	0.22	*0.324	*15.2
3	6.51	30.34	47.05	21.59	...	*0.207	*0.5
4	46.19	33.91	48.80	8.57	4.69	0.794	5.3
5	33.59	11.90	48.07	5.95	...	*0.453	*4.6
6	20.84	25.06	47.98	10.97	0.77	0.422	2.1
7	10.95	16.11	47.23	12.13	...	*0.237	*1.1
8	12.90	33.98	47.70	16.23	...	*0.339	*1.1
9	23.30	45.84	48.34	14.03	0.33	0.556	2.1
10	7.21	44.38	47.30	24.82	5.94	0.251	0.5
11	13.85	28.75	47.68	14.41	...	*0.337	*1.2
12	6.54	28.68	47.03	20.95	30.27	0.097	0.8
13	4.79	88.33	47.25	42.92	72.90	0.064	0.7
14	40.83	1.39	47.31	1.85	9.97	0.253	10.1
15	6.66	24.78	46.98	19.29	73.46	0.052	1.4
16	8.02	68.02	47.58	29.12	73.96	0.082	1.4
17	12.22	11.28	47.17	9.61	...	*0.227	*1.3
18	9.17	22.45	47.22	15.65	16.66	0.168	1.0
19	24.94	183.33	48.99	27.11	244.93	0.109	8.0
20	*20.36	*5.88	*47.33	*5.37	6.66	*0.257	*3.0
21	17.85	74.51	48.32	20.43	182.20	0.079	5.7
22	15.02	384.53	48.86	50.60	157.61	0.132	2.9
23	16.00	87.68	48.29	23.41	184.11	0.077	4.8
24	*8.63	*402.88	*48.39	*68.31	95.39	*0.129	*1.1
25	4.90	48.99	47.01	31.62	106.05	0.042	1.0
26	8.70	11.39	46.88	11.44	37.11	0.076	1.7
27	11.41	188.10	48.32	40.61	44.63	0.202	1.3
28	23.58	53.78	48.42	15.10	3.03	0.591	2.0
29	10.91	11.93	47.10	10.45	3.11	0.214	1.1
30	11.05	11.35	47.09	10.14	13.64	0.173	1.4
31	27.61	6.74	47.66	4.94	4.72	0.329	4.2
32	8.87	20.04	47.14	15.03	10.94	0.209	0.8
33	8.06	26.49	47.18	18.13	2.72	0.228	0.6
34	*26.73	*2.49	*47.20	*3.05	2.25	*0.231	*5.1
35	*13.66	*0.64	*46.02	*2.16	1.35	*0.094	*3.1
36	17.30	10.80	47.45	7.90	...	*0.282	*2.1
37	*13.66	*1.25	*46.31	*3.02	0.92	*0.117	*2.6
38	15.30	15.95	47.52	10.21	2.51	0.296	1.6
39	*18.18	*0.31	*45.95	*1.30	0.67	*0.089	*5.4
40	20.22	8.74	47.50	6.58	1.93	0.292	2.7
41	*49.30	*2.37	*47.71	*2.19	0.64	*0.342	*11.2
42	*26.73	*0.56	*46.54	*1.44	0.21	*0.140	*7.5
43	*22.51	*0.44	*46.30	*1.41	0.58	*0.116	*6.4
44	18.18	1.12	46.51	2.48	18.89	0.090	5.3
45	*24.63	*0.74	*46.60	*1.73	0.56	*0.146	*6.3
46	21.03	46.73	48.26	14.91	...	*0.522	*1.8
47	*22.51	*0.43	*46.28	*1.38	0.97	*0.115	*6.4
48	6.51	106.80	47.59	40.51	66.06	0.089	0.9
49	12.39	131.78	48.24	32.62	26.56	0.269	1.2
50	7.28	14.09	46.82	13.92	0.61	0.173	0.7
51	30.47	39.57	48.51	11.39	...	*0.633	*3.0
52	10.35	23.94	47.35	15.21	...	*0.261	*0.9
53	*32.96	*1.65	*47.20	*2.23	0.65	*0.232	*7.4
54	*77.55	*0.25	*47.12	*0.56	...	*0.218	*34.7

Notes. *: Sources that are without detection in 22.4 GHz. Parameters are derived from 6 GHz flux and the deconvolved core size. †: No detection in 96 GHz. Parameters are derived assuming $n_{\text{H}_2} = 2 \times 10^7$ cm $^{-3}$

Table B.3. Which cores in [Ginsburg et al. \(2018\)](#) are associates with outflows.

ID	Outflow	ID	Outflow	ID	Outflow	ID	Outflow	ID	Outflow	ID	Outflow
1	Y	47	–	97	–	143	N	202	–	258	Y
2	Y	48	–	98	–	144	N	203	–	259	Y
3	Y	49	Y	99	–	145	–	204	–	260	Y
4	Y	50	Y	100	–	146	–	205	–	261	N
5	Y	51	Y	102	–	147	N	206	–	262	N
6	N	52	–	103	–	148	–	207	Y	263	N
7	Y	53	–	104	–	149	–	208	N	266	N
8	Y	54	Y	105	–	150	–	209	N	267	N
9	N	55	–	106	–	153	–	210	Y	268	N
10	N	56	–	107	–	154	–	211	Y	269	N
11	N	57	–	108	–	155	–	212	Y	270	N
12	Y	58	–	109	–	156	–	213	–	271	N
13	–	59	–	110	–	157	–	214	–	101_X	–
14	N	60	–	111	–	158	Y	215	–	175_G	–
15	–	61	–	112	–	159	Y	216	–	177_B	–
16	Y	62	–	113	–	160	Y	217	–	180_E	–
17	Y	63	–	114	–	161	Y	218	–	181_D	–
18	Y	64	–	115	–	162	Y	219	–	182_Y	–
19	Y	65	–	116	N	163	Y	220	–	244_C	–
20	Y	66	–	117	N	164	–	221	–	265_H	N
21	N	67	–	118	N	165	–	222	–	171_K3	–
22	Y	68	–	119	–	166	–	223	–	172_K2	–
23	Y	69	–	120	Y	167	–	224	–	173_K1	–
24	Y	70	N	121	N	168	–	226	–	174_f3	–
25	Y	71	N	122	N	169	–	227	–	176_f1	–
26	–	72	N	123	N	170	–	228	–	234_f4	–
27	–	73	N	124	N	183	N	229	–	235_f2	–
28	–	74	N	125	N	184	N	230	–	245_A2	–
29	–	75	N	126	N	185	N	231	–	264_k4	–
30	–	76	N	127	N	186	N	232	–	86_B9.96	–
31	–	77	N	128	N	187	N	238	–	87_B9.99	–
32	–	78	N	129	N	188	N	239	–	90_B9.89	–
33	–	79	N	130	–	189	N	243	–	92_I10.52	–
34	Y	80	N	131	–	190	N	246	–	96_Z10.24	–
35	Y	81	N	132	–	191	N	247	–	151_B10.06	–
36	Y	82	N	133	–	192	N	248	N	152_f10.32	–
37	N	83	N	134	–	193	N	249	N	178_f10.37	–
38	Y	84	–	135	–	194	N	250	–	179_f10.38	–
39	–	85	–	136	–	195	Y	251	–	237_G10.44	–
40	–	88	–	137	–	196	Y	252	–	241_f10.30	–
41	–	89	–	138	–	197	Y	253	–	225_f10.33b	–
42	–	91	–	139	–	198	Y	254	N	233_f10.27b	–
43	–	93	–	140	Y	199	–	255	N	236_f10.303	–
44	–	94	–	141	Y	200	–	256	Y	240_f10.44b	–
45	Y	95	–	142	–	201	–	257	Y	242_f10.318	–
46	Y	–	–	–	–	–	–	–	–	–	–

Notes. The IDs of the dust cores are as in Table 3 in [Ginsburg et al. \(2018\)](#). Cores that are not covered by the SiO image (Fig. C.2) are marked “–”. Cores that are covered by the SiO image and associated or not associated with outflows are flagged Y or N, respectively.